Towards the modelling of ageing and atherosclerosis effects in ApoE$^{-/-}$ mice aortic tissue

Tobias Waffenschmidt [a,g], Myriam Cilla [b], Pablo Sáez [d], Marta M. Pérez [e],
Miguel A. Martínez [c], Andreas Menzel [a,f], Estefanía Peña [c,*]

[a]*Institute of Mechanics, Department of Mechanical Engineering, TU Dortmund, Germany*

[b]*Centro Universitario de la Defensa, Academia General Militar, Zaragoza, Spain*

[c]*Applied Mechanics and Bioengineering, Aragón Institute of Engineering Research (I3A), University of Zaragoza, CIBER de Bioingeniería, Biomateriales y Nanomedicina (CIBER-BBN), Spain*

[d]*Laboratori de Calcul Numeric (LaCaN), Universitat Politecnica de Catalunya, Barcelona, Spain*

[e]*Department of Anatomy, Embryology and Genetics, Veterinary Faculty, University of Zaragoza*

[f]*Division of Solid Mechanics, Lund University, Sweden*

[g]*3M Deutschland GmbH, Carl-Schurz-Str. 1, D-41453 Neuss, Germany*

Abstract

The goal of this work consists in a quantitative analysis and constitutive modelling of ageing processes associated to plaque formation in mice arteries. Reliable information on the characteristic evolution of pressure-stretch curves due to the ageing effects are extracted from previous inflation test experiments. Furthermore, characteristic age-dependent material parameters are identified on the basis of a continuum-mechanics-based parameter optimisation technique.

The results indicate that the aorta-stiffness of the healthy control mice remains basically constant irrespective of the diet-time and age. In contrast, significant differences exist within the material response and in consequence within the material parameters between the ApoE$^{-/-}$ and the control mice as well as for the different locations over the aorta which is underlined by our experimental observations. With regard to the temporal evolution of the material parameters, we observe that the material parameters for the ApoE$^{-/-}$ mice aortas exhibit a saturation-type increase with respect to age.

Key words: Ageing, anisotropic biological tissues, thick-walled tube, parameter identification.

* Corresponding author. Estefanía Peña. Mechanical Engineering Department. c/ Maria de Luna s/n

50018. Zaragoza. Spain. Tel.: +34 876555233; Fax: +34 976762578

Email address: `fany@unizar.es` (Estefanía Peña).

1 Introduction

Recent experimental studies have shown that atherosclerosis significantly modifies the mechanical properties of the arterial tissue (Teng et al., 2014). In this regard, a combination of inflammatory, biological and mechanical processes tends to remodel the arterial wall structure and composition (Tracqui et al., 2011). Manifold animal species are commonly used to study the pathogenesis and potential treatment of the lesions of atherosclerosis (Buja et al., 1983; Faggiotto et al., 1984; Reitman et al., 1982; Schwartz et al., 1985; Wagner, 1978). Experimental tests on mice over a period of several months can be carried out and results may be extrapolated for the benefit of middle-aged or elderly humans.

Studying the mechanical properties during atheroma plaque development is particularly important in order to understand the mechanisms of vascular adaptation in response to changes in physical stress. Several studies investigate the morphological, structural, and biochemical changes of the aorta as well as the relation between these changes and the mechanics of the aorta (Davis, 1995; Huang et al., 2006; Machii and Becker, 1997; Wells et al., 1999; Wong and Langille, 1996; Tsamis et al., 2013). Most of these studies, however, mainly focus on the proximal aorta, and none of them systematically characterise the geometrical and mechanical properties along the entire length of the aorta. Even though Guo and Kassab (2003) study the whole aorta, they exclusively focus on the standard laboratory mice (C57BL/6J mice).

The modelling, simulation and experimental study of arteries and associated vascular diseases such as atherosclerosis is an area of current multidisciplinary research. In order to enable an individual patient-specific adaptation/modification of the medical treatment, it is necessary to understand the underlying mechanisms of atherosclerotic plaque evolution. In this context, modelling and simulation are becoming increasingly important research topics (Cilla et al., 2014). As *in-vivo* experiments are usually not feasible for the study of human arteries, both

modelling and simulation of ageing phenomena have become vital for the improvement of the reliability of medical prognoses. For the description of the purely mechanical and passive behaviour of arteries, several computational material models have already been developed in the past decades (Holzapfel et al., 2000). In this context, we consider continuum mechanics models and numerical approaches to validate and calibrate our constitutive models based on the experimental investigations. However, the temporal evolution in these vessels, commonly referred to as ageing, has hardly been discussed in the literature. Nevertheless, the incorporation of such ageing effects—in combination with the detection, description, and especially interaction with plaques—is of central importance for the understanding of atherosclerosis.

The scientific goal of this work is the mechanical analysis and constitutive modelling of ageing processes usually associated with plaque formation in mouse arteries. Specifically speaking, reliable information on the evolution of pressure-stretch curves due to ageing effects is extracted from previous experimental investigations (Cilla et al., 2015). A computational mechanics framework is used to identify age-dependent material parameters on the basis of the experimental data. We consider an inhomogeneous boundary value problem at large deformations for an incompressible thick-walled cylindrical tube, which is assumed to be a rough approximation for a real artery.

2   Materials and methods

2.1   Mechanical tests

Female apolipoprotein E-deficient transgenic mice (ApoE$^{-/-}$ mice) and common laboratory control mice (C57BL/6 mice) are used to obtain the pressure-diameter relation (Cilla et al., 2015). We analyse the progressive evolution of atherosclerotic lesions at three different locations of the aorta of (i) ApoE$^{-/-}$ mice put on a hyper-lipidic Western diet and (ii) C57BL/6 control

3

$_{48}$ mice put on a normal chow diet. Different sets of five ApoE$^{-/-}$ and control mice are sacrificed

$_{49}$ after 10, 20, 30 and 40 weeks.

$_{50}$ Inflation tests are performed as described in Cilla et al. (2015). The aorta is preconditioned

$_{51}$ within three cycles from $0\,[mmHg] - 200\,[mmHg]$. Thereafter, the perfusion pressure p_i is

$_{52}$ increased in steps of $25\,[mmHg]$ from $p_i = 0\,[mmHg] - 250\,[mmHg]$, (Guo and Kassab, 2003),

$_{53}$ while the outer diameter d_o along the trunk of the aorta at each pressure step is recorded. The

$_{54}$ blood vessel is subdivided into a series of short regions of approximately $3\,[mm] - 4\,[mm]$ length

$_{55}$ per segment, and the external diameter and circumferential stretch are both measured point-

$_{56}$ wise. The outer circumferential stretch is evaluated as the ratio of the current and referential

$_{57}$ outer diameters d_o and D_o, i.e. $\lambda_{\theta_o} = \frac{d_o}{D_o}$, details on Cilla et al. (2015).

$_{58}$ An average pressure-circumferential-stress-relation for each of the segments is measured. Three

$_{59}$ different zones of the aorta are studied separately, i.e. the upper thoracic aorta, the lower

$_{60}$ thoracic aorta and the abdominal aorta. The upper thoracic zone is considered **to reach from**

$_{61}$ **the aortic arch to the ninth thoracic vertebra, the lower thoracic up to the superior**

$_{62}$ **mesenteric branch and the abdominal part from there to the iliac bifurcation.** They

$_{63}$ are not identical to ascending and descending thoracic aorta. The objective was to divide the

$_{64}$ aorta in regions of similar lengths. This description of the upper and lower thoracic aorta is

$_{65}$ included in the new version of the manuscript.

$_{66}$ *2.2   Computational framework*

$_{67}$ We propose a computational mechanics framework to identify age-dependent material param-

$_{68}$ eters of the data obtained by the experimental tets.

2.2.1   Kinematics

70 Position vectors of particles in an undeformed reference configuration $\mathcal{B}_0$ are denoted by $\boldsymbol{X}$

71 and position vectors in the deformed current configuration $\mathcal{B}_t$ at time t by $\boldsymbol{x} = \boldsymbol{\varphi}(\boldsymbol{X}, t)$. The

72 kinematics of a thick-walled tube can conveniently be described by cylindrical polar coordinates.

73 These coordinates are introduced as R, Θ and Z with respect to a chosen reference configuration

74 $\mathcal{B}_0$ as well as r, θ and z with respect to the current configuration $\mathcal{B}_t$. An orthonormal referential

75 and spatial frame, respectively, can be defined in terms of these coordinates as

$$\boldsymbol{E}_R(\Theta) = \quad \cos(\Theta)\,\boldsymbol{e}_1 + \sin(\Theta)\,\boldsymbol{e}_2\,, \qquad \boldsymbol{e}_r(\theta) = \quad \cos(\theta)\,\boldsymbol{e}_1 + \sin(\theta)\,\boldsymbol{e}_2\,, \qquad (1)$$

$$\boldsymbol{E}_\Theta(\Theta) = -\sin(\Theta)\,\boldsymbol{e}_1 + \cos(\Theta)\,\boldsymbol{e}_2\,, \qquad \boldsymbol{e}_\theta(\theta) = -\sin(\theta)\,\boldsymbol{e}_1 + \cos(\theta)\,\boldsymbol{e}_2\,, \qquad (2)$$

$$\boldsymbol{E}_Z \quad = \quad \boldsymbol{e}_3\,, \qquad \boldsymbol{e}_z \quad = \quad \boldsymbol{e}_3\,. \qquad (3)$$

76 wherein $\{\boldsymbol{e}_1, \boldsymbol{e}_2, \boldsymbol{e}_3\}$ is a Cartesian frame fixed in space. The geometry of the tube considered

77 is visualised in Figure 1 and its material and spatial settings are specified by

78   [Fig. 1 about here.]

$$R_i \leq R \leq R_o\,, \qquad r_i \leq r \leq r_o\,, \qquad (4)$$

$$0 \leq \Theta \leq 2\pi\,, \qquad 0 \leq \theta \leq 2\pi\,, \qquad (5)$$

$$0 \leq Z \leq L\,, \qquad 0 \leq z \leq l\,, \qquad (6)$$

79 where R_i, R_o and L represent the inner and outer radii and the length of the tube in a (unde-

80 formed) reference configuration $\mathcal{B}_0$, while r_i, r_o and l represent the corresponding quantities in

81 the (deformed) current configuration $\mathcal{B}_t$; see Figure 1. The deformation modes of inflation and

82 extension of an incompressible tube can be represented by the spatial position vector

$$\boldsymbol{x} = \boldsymbol{\varphi}(\boldsymbol{X}, t) = r\,\boldsymbol{e}_r(\theta) + z\,\boldsymbol{e}_z \tag{7}$$

specified by means of

$$r = \sqrt{\frac{R^2 - R_i^2}{\lambda_z} + r_i^2}\,, \qquad \theta = \Theta\,, \qquad z = \lambda_z\,Z\,, \tag{8}$$

where λ_z represents the axial stretch.

Representative deformation measures can be introduced with respect to the coordinates R, Θ, Z and r, θ, z. In particular, equation (7) is used together with $\nabla_{\boldsymbol{X}}\,[\bullet] = \partial_R\,[\bullet] \otimes \boldsymbol{E}_R + R^{-1}\,\partial_\Theta\,[\bullet] \otimes \boldsymbol{E}_\Theta + \partial_Z[\bullet] \otimes \boldsymbol{E}_Z$ to introduce the deformation gradient $\boldsymbol{F} = \nabla_{\boldsymbol{X}}\,\boldsymbol{\varphi}$. For the present scenario, the deformation gradient reduces to

$$\boldsymbol{F} = \lambda_r\,\boldsymbol{e}_r \otimes \boldsymbol{E}_R + \lambda_\theta\,\boldsymbol{e}_\theta \otimes \boldsymbol{E}_\Theta + \lambda_z\,\boldsymbol{e}_z \otimes \boldsymbol{E}_Z\,, \tag{9}$$

where the radial and circumferential stretch are each introduced as

$$\lambda_r = \frac{R}{r\,\lambda_z} \qquad \text{and} \qquad \lambda_\theta = [\lambda_r\lambda_z]^{-1} = \frac{r}{R}\,. \tag{10}$$

λ_r, λ_θ and λ_z take the interpretation as principal stretches in radial, circumferential and axial direction.

2.2.2 Constitutive model

We apply an orthotropic model with two families of fibres as introduced by Holzapfel et al. (2000). The strain energy function of this model is assumed to additively decompose into an isotropic part Ψ_{iso}, representing the contribution of the non-collagenous ground material, and into an anisotropic part Ψ_{ani}, representing the contributions of the different families of collagen fibres, i.e.

$$\Psi(\boldsymbol{F}, \boldsymbol{a}_{0\,i}) = \Psi_{\text{iso}}(\boldsymbol{F}) + \Psi_{\text{ani}}(\boldsymbol{F}, \boldsymbol{a}_{0\,i})\,. \tag{11}$$

Moreover, $\boldsymbol{a}_{0\,i}$ denotes a set of $i = 1, \ldots, N$ referential unit-vectors characterising the mean orientations of the fibre families. The isotropic part of the strain energy is specified by a common neo-Hookean format

$$\Psi_{\text{iso}}(\boldsymbol{F}) = \frac{c}{2}\left[I_1 - 3 \right], \tag{12}$$

with $I_1 = \boldsymbol{F} : \boldsymbol{F} = \lambda_\theta^2 + \lambda_z^2 + \lambda_\theta^{-2}\lambda_z^{-2}$ for the incompressible case, i.e. $J = \det(\boldsymbol{F}) \doteq 1$. The anisotropic part adopted takes the following exponential form

$$\Psi_{\text{ani}}(\boldsymbol{F}, \boldsymbol{a}_{0\,i}) = \frac{k_1}{2\,k_2} \sum_{i=1}^{N} \left[\exp\left(k_2 \,\langle E_i \rangle^2 \right) - 1 \right], \tag{13}$$

wherein it is assumed that the fibres are mechanically equivalent. The notation $\langle \bullet \rangle = [\, |\bullet| + \bullet\,]/2$ reflects the Macaulay brackets. These allow the activation of the fibre contributions in the tension regime only. A referential strain measure E_i is introduced as

$$E_i = \boldsymbol{a}_{0\,i} \cdot \boldsymbol{F}^{\text{t}} \cdot \boldsymbol{F} \cdot \boldsymbol{a}_{0\,i} - 1 = I_{4\,i} - 1\,. \tag{14}$$

The number of mechanically equivalent fibre families is restricted to $N = 2$ and, moreover, their initial orientations are assumed as

$$\boldsymbol{a}_{0\,1,2} = \sin(\beta)\,\boldsymbol{E}_Z \pm \cos(\beta)\,\boldsymbol{E}_\Theta\,, \tag{15}$$

so that the invariant introduced in equation (14) can be expressed as

$$I_{4\,i} = \boldsymbol{a}_{0\,i} \cdot \boldsymbol{F}^{\text{t}} \cdot \boldsymbol{F} \cdot \boldsymbol{a}_{0\,i} = \sin^2(\beta)\,\lambda_z^2 + \cos^2(\beta)\,\lambda_\theta^2\,. \tag{16}$$

7

With these relations at hand, the Cauchy stress tensor $\boldsymbol{\sigma} = J^{-1} \partial_{\boldsymbol{F}} \Psi \cdot \boldsymbol{F}^{\mathrm{t}}$ can be specified, namely

$$\boldsymbol{\sigma} = c\,\boldsymbol{F} \cdot \boldsymbol{F}^{\mathrm{t}} + 4\,k_1\,E \exp\left(k_2\,\langle E \rangle^2\right) [\,\boldsymbol{a}_1 \otimes \boldsymbol{a}_1 + \boldsymbol{a}_2 \otimes \boldsymbol{a}_2\,], \tag{17}$$

with $\boldsymbol{a}_{1,2} = \boldsymbol{F} \cdot \boldsymbol{a}_{0\,1,2}$, and spectral form

$$\sigma_{rr} = c\,\lambda_\theta^{-2}\,\lambda_z^{-2}\,, \tag{18}$$

$$\sigma_{\theta\theta} = c\,\lambda_\theta^2 + 4\cos^2(\beta)\,k_1\,\lambda_\theta^2\,E \exp\left(k_2\,\langle E \rangle^2\right)\,, \tag{19}$$

$$\sigma_{zz} = c\,\lambda_z^2 + 4\sin^2(\beta)\,k_1\,\lambda_z^2\,E \exp\left(k_2\,\langle E \rangle^2\right)\,. \tag{20}$$

2.2.3 Equilibrium conditions

Neglecting body forces, the underlying local equilibrium conditions in terms of spatial arguments take the representation as

$$\boldsymbol{0} = \nabla_{\boldsymbol{x}} \cdot \boldsymbol{\sigma} \qquad \text{in} \quad \mathcal{B}_t\,, \tag{21}$$

$$\boldsymbol{t} = \boldsymbol{\sigma} \cdot \boldsymbol{n} \qquad \text{on} \quad \partial\mathcal{B}_t\,, \tag{22}$$

$$\boldsymbol{t} = -\,p_i\,\boldsymbol{n} \qquad \text{on} \quad \partial\mathcal{B}_{ti}\,. \tag{23}$$

By analogy with the derivations reviewed above and with $\boldsymbol{n} = \pm\,\boldsymbol{e}_r$, the Euler-Lagrange equations can be summarised as

8

$$\mathbf{0} = \left[\frac{\partial \sigma_{rr}}{\partial r} + \frac{\sigma_{rr} - \sigma_{\theta\theta}}{r} \right] \boldsymbol{e}_r + \frac{1}{r} \frac{\partial \sigma_{\theta\theta}}{\partial \theta} \boldsymbol{e}_\theta + \frac{\partial \sigma_{zz}}{\partial z} \boldsymbol{e}_z \qquad \text{in} \quad \mathcal{B}_t \, , \tag{24}$$

$$\boldsymbol{t} = \sigma_{rr} \, \boldsymbol{e}_r \qquad\qquad\qquad \text{on} \ \ \partial \mathcal{B}_{to} \, , \tag{25}$$

$$\boldsymbol{t} = p_i \, \boldsymbol{e}_r \qquad\qquad\qquad \text{on} \ \ \partial \mathcal{B}_{ti} \, . \tag{26}$$

117 Due to geometrical and constitutive symmetry, the only non-trivial component of (24) is

$$\frac{\partial \sigma_{rr}}{\partial r} + \frac{\sigma_{rr} - \sigma_{\theta\theta}}{r} = 0 \, , \tag{27}$$

118 see, for example, Ogden (1997). From this equation and from boundary condition $\sigma_{rr}|_{r=r_o} = 0$

119 on the outer surface of the tube, the radial Cauchy stress σ_{rr} may be calculated as

$$\sigma_{rr}(\xi) = \int_\xi^{r_o} [\sigma_{rr} - \sigma_{\theta\theta}] \frac{\mathrm{d}\xi}{\xi} \, . \tag{28}$$

120 The internal pressure $p_i = -\sigma_{rr}|_{r=r_i}$ is then obtained in the form

$$p_i = \int_{r_i}^{r_o} [\sigma_{\theta\theta} - \sigma_{rr}] \frac{\mathrm{d}r}{r} \, . \tag{29}$$

121 *2.2.4 Material parameter identification*

122 The objective is to determine the characteristic evolution of material parameters in time on

123 the basis of the experimental measurements. Several assumptions and approximations are in-

124 cluded into the model. First, we idealise the aortic geometry by adopting a thick-walled tube

125 and a single layer. Secondly, we replicate the experimental setting by imposing boundary con-

126 ditions and kinematic constraints: fully incompressible, uniform internal pressure at the inner

127 diameter, stress-free at the outer diameter of the tube (the outer circumferential stretch λ_{θ_o}

128 is one for zero pressure for all experimental pressure-stretch-curves), constant axial residual

stretch, and circumferential residual stretch neglected. Thirdly, we adopt the following consti-

tutive assumptions: hyperelastic (inelastic effects neglected), anisotropic (transversely isotropic

or orthotropic), two mechanically equivalent families of fibres, fibres oriented in tangential plane

of the tube, non-zero mechanical response of the fibres in tension-regime only, fibre dispersion

neglected, and homogeneous material properties.

[Table 1 about here.]

In order to investigate the age-dependent evolution of the material parameters in detail, we

first fit the material parameters associated with the constitutive model to the pressure-outer-

circumferential-stretch curves recorded during the experiments (p_i-λ_{θ_o}-curves).

For the computational fitting process, we apply a pressure-driven parameter identification pro-

cedure where, by analogy to the experimental approach, the internal pressure p_i^{exp} is applied

to the tube, see Table 2 for algorithmic details. The equilibrium condition (24) is not fulfilled

a priori and therefore requires an additional iterative solution procedure. We apply a com-

mon Newton-Raphson iteration scheme to iteratively satisfy the equilibrium condition of the

underlying boundary value problem as summarised in Table 2. This enables us to compute

an objective function f formulated in terms of the stretch-difference $\lambda_{\theta_o} - \lambda_{\theta_o}^{\mathrm{exp}}$. The objective

function is then minimised with respect to the material parameters $\boldsymbol{\nu}$, see Table 3. Generally,

such minimisation problems may conveniently be solved by typical optimisation techniques. In

this study, the Matlab optimisation-algorithm `fmincon` is used which is based on a sequential

quadratic programming (SQP) method. We end up with a set of material parameters $\boldsymbol{\nu}^{\mathrm{min}}$

providing optimal data fitting capabilities for the particular experimental curve of interest.

[Table 2 about here.]

[Table 3 about here.]

10

152 The material parameter identification procedure is based on a sequential optimisation of three

153 material parameters c, k_1 and k_2 as described in Sáez et al. (2014). In a first step, parameter

154 c is identified with $k_1 = $ const and $k_2 = $ const using the first two experimental data points,

155 in a second step k_1 and k_2 are identified with $c = $ const using all experimental data points.

156 This non-standard sequential optimisation technique was applied, as it may occur that a single

157 optimisation including every experimental data point for all of the three material parameters

158 results in unphysical material parameters, e.g. such that $c < 0$, or in $c = \texttt{lb}$ for a constrained

159 optimisation including a lower bound $\texttt{lb}$.

160 [Table 4 about here.]

161 Finally, we end up with a set of material parameters $\boldsymbol{\nu}^{min}$ providing optimal data fitting ca-

162 pabilities for the particular experimental curve of interest. The identified material parameters

163 are then plotted over time/age in order to obtain an impression as to which parameter might

164 be less/more affected due to the ageing effects.

165 ## 3   Results

166 *3.1   Mechanical properties*

167 In order to illustrate the stiffening behaviour with respect to age, (Figure 2) shows the ex-

168 perimentally obtained circumferential stretch over different stages of ageing at three chosen

169 pressure levels, i.e. $p_i = \{50, 150, 250\}\,[mmHg]$.

170 We observed that the circumferential stretch λ_{θ_o} decreases with age (stiffening) for the diseased

171 ApoE$^{-/-}$ mice but stays relatively constant for the healthy control mice.

172 [Fig. 2 about here.]

11

173 As pointed out by Cilla et al. (2015), the $\text{ApoE}^{-/-}$ mice aorta stiffness increases dramatically

174 with an increasing diet period. This holds for all the aortic zones studied. In contrast, the aorta

175 stiffness of the control mice remains relatively constant for an increasing diet period. Comparing

176 the $\text{ApoE}^{-/-}$ and control results, the $\text{ApoE}^{-/-}$ pressure-stretch curves after 10 $[weeks]$ for the

177 upper aorta and after 10 and 20 $[weeks]$ for the lower and abdominal aorta are similar to the

178 control curves for all ages.

179 *3.2 Material parameter identification*

180 The material parameters, i.e. c, k_1 and k_2, which characterise the mechanical response of the

181 artery are expected to evolve in time due to the ageing process. The fitting results of the

182 material parameter identification procedure are depicted in Figure 3. The results in Figure 3

183 show excellent fitting capabilities.

184   [Fig. 3 about here.]

185   [Table 5 about here.]

186 The identified material parameters are summarised in Table 5 and their temporal evolution is

187 illustrated in Figure 4. With regard to the temporal evolution of the material parameters, we

188 expected the material parameters for the control mice to remain almost constant for a specific

189 location of the aorta. However, the parameters strongly deviate from each other with respect to

190 time, see parameter k_2 in Figure 4. We also expected the material parameters for the $\text{ApoE}^{-/-}$

191 mice aortas to exhibit a characteristic increase or decrease in time for one single location. And

192 we indeed observe that, e.g. parameter c first increases linearly within $t = 10 - 30\,[weeks]$

193 and saturates for $t = 30 - 40\,[weeks]$. A similar behaviour holds for parameter k_1, whereas k_2,

194 remains almost constant within $t = 10 - 30\,[weeks]$ and then increases for $t = 30 - 40\,[weeks]$,

195 see Figure 4.

12

4 Discussion

A computational mechanics framework is used to identify age-dependent material parameters on the basis of the experimental data. We consider an inhomogeneous boundary value problem that allows for large deformations, i.e. an incompressible thick-walled cylindrical tube, which is assumed to approximate a real artery. The basic deformation modes considered are represented by combined inflation and axial extension. We make use of an orthotropic constitutive model with two families of fibres and solve the underlying equilibrium conditions iteratively. We compute an objective function, represented by the difference between simulated and experimental data, which is minimised with respect to the material parameters. As a main goal, we aim at determining the characteristic age-dependent evolution of the material parameters over time. Generally, the results show excellent fitting capabilities. Similar results have previously been obtained by (Cheng et al., 2013). They used a fibre-based constitutive model to fit the mechanical properties from the aorta during postnatal development of wild-type mice and elastin haploinsufficient (Eln+/-) mice. Their results showed that a similar fibre-based constitutive model was capable of distinguishing elastin content during development.

We observe significant deviations of the material parameters between the ApoE$^{-/-}$ and the control mice as well as for the different locations over the aorta (upper, lower, abdominal) which clearly underline our observations from the experiments. With regard to the temporal evolution of the material parameters, we identify the material parameters for the control mice aortas for one single location to remain almost constant. However, it becomes apparent that the parameters quite strongly deviate from each other with respect to position mainly k_2. We reporte the material parameters for the ApoE$^{-/-}$ mice aortas for one single location to exhibit a characteristic increase/decrease in time. We indeed observe that parameter c first increase

13

linearly and saturate for $t = 30 - 40 \, [weeks]$. c **parameter is the principle determinant of stiffness in the small stretch region (pressure below physiological level), where the crimped collagen molecules are primarily weaving. However, if there is a rupture of the elastin, there is no the transition region between the elastin-dominated and the collagen-dominated parts of the stress-strain response, thus indicating earlier collagen recruitment. For that reason, there is an increasing of the slope of the stress-strain curve, so there is an increasing of the c parameter. This effect is due to fragmentation of the elastin due to atherosclerosis and not due to ageing where the content of elastin remains unaltered with age; however, its concentration is de-creased (Tsamis et al., 2013). A similar behaviour can be identified for parameter k_1, this parameter is the principle determinant of collagen stiffness in the small stretch region of the stress-strain response, where the collagen molecules are pri-marily straightened and the tissue is resilient.** Whereas k_2 remained almost constant within $t = 10 - 30 \, [weeks]$ and then increased for $t = 30 - 40 \, [weeks]$. The main reason for this fact could be that forty weeks may not suffice in order to study representative age-related changes in elastic behavior for control groups, and that forty weeks is the start point of the ageing process. However, additional studies are needed to understand and check this hypothesis. **Similar results were found on humans by Astrand et al. (2011).**

To the best of the author's knowledge, not many studies containing all these characteristics appear to be available in the literature. Only Agianniotis and Stergiopulos (2012b) have so far compared the mechanical properties of young 10-12 week-old ApoE$^{-/-}$ mice without fat diet with C57BL/6J wild-type mice by extension-inflation mechanical tests. In their work, particular emphasis was placed on the computation of the Hudetz incremental elastic modulus. Previous studies suggest that 10% of collagen fibres are engaged at physiological pressure (Greenwald et al., 1997), whereas at higher pressures, the blood vessel becomes progressively less distensible as collagen fibres are recruited to support passive wall tension and to restrict aortic distension.

The pulse wave velocity increasement on ApoE$^{-/-}$ matches to the fragmentation of the elastic laminae in the arterial wall.

It should be pointed out that the study presented here contains some assumptions and limitations. First, the application of an inhomogeneous incompressible thick-walled cylindrical tube which should represent a real artery is a significant idealisation and simplification. For future studies, a non-cylindrical multi-layered problem setting should at least be considered. However, the number of fitting parameters will increase, and to gain a realistic interpretation of their physical sense some layer-specific information will be required. The assumption of circumferential uniformity seems to be different between ApoE$^{-/-}$ mice, which have numerous plaques concentrated around branches, and control mice, where the wall is much more uniform. The plaques and geometry can influence the mechanical behaviour of the vessel and therefore distort results due to the heterogeneous and inconsistent nature of their development. However, Tracqui et al. (2011) measured the stiffness of the mice plaque and obtained much lower values with respect to the vessel wall, so its effect on mechanical properties could be lower than expected.

In addition, material parameters can also be introduced as functions in time. To keep the fitting problem as simple as possible in order to avoid coupled mechanical effects, we did not consider residual stretches. Although some investigations have previously been carried out to study the aperture angle, these data cannot be uniquely related to the increase of residual stresses. Moreover, circumferential residual stretches essentially require the acquisition of related experimental data which, in turn, is a non-trivial task and therefore not achievable at this stage. In addition since these inflation tests are performed *in situ*, the measurement of longitudinal forces, and thus the longitudinal stiffness cannot be assessed.

In spite of these limitations, the obtained results are promising and demonstrate substantial changes in the mechanical properties of ApoE$^{-/-}$ mice aortas when compared to the results obtained from the control mice group. These findings are important for a better understanding

15

of the cardiovascular system of mice and could serve as a reference for future investigations of mechanical properties of blood vessels suffering atherosclerotic diseases.

5 Acknowledgements

6 Conflict of interest

None of the authors of this work has conflict of interest with other people and organisations.

References

Agianniotis, A., Stergiopulos, N., 2012b. Wall properties of the apolipoprotein E-deficient mouse aorta. Atherosclerosis 223 (2), 314–320.

Astrand, H., Stalhand, J., Karlsson, J., Karlsson, M., Sonesson, B., , Länne, T., 2011. In vivo estimation of the contribution of elastin and collagen to the mechanical properties in the human abdominal aorta: effect of age and sex. J Appl Physiol 110, 176–187.

Buja, L., Kita, T., Goldstein, J., Watanabe, Y., Brown, M., 1983. Cellular pathology of progressive atherosclerosis in the WHHL rabbit. An animal model of familial hypercholesterolemia. Arteriosclerosis, Thrombosis, and Vascular Biology 3 (1), 87–101.

Cheng, J. K., Stoilov, I., Mecham, R. P., Wagenseil, J. E., 2013. A fiber-based constitutive

16

model predicts changes in amount and organization of matrix proteins with development and disease in the mouse aorta. Biomech Model Mechanobiol 12, 497–510.

Cilla, M., Peňa, E., Martínez, M. A., 2014. Mathematical modelling of atheroma plaque formation and development in coronary arteries. J R Soc Interface 11, 20130866 1–16.

Cilla, M., Pérez, M. M., Peňa, E., Martínez, M. A., 2015. Effect of diet and age on arterial stiffening due to atherosclerosis in ApoE$^{-/-}$ mice. Ann Biomed Eng In press.

Davis, E. C., 1995. Elastic lamina growth in the developing mouse aorta. Journal of Histochemistry & Cytochemistry 43 (11), 1115–23.

Faggiotto, A., Ross, R., Harker, L., 1984. Studies of hypercholesterolemia in the nonhuman primate. I. Changes that lead to fatty streak formation. Arteriosclerosis, Thrombosis, and Vascular Biology 4 (4), 323–340.

Greenwald, S. E., Moore, J. E. J., Rachev, A., Kane, T., Meister, J. J., 1997. Experimental investigation of the distribution of residual strains in the artery wall. ASME Journal of Biomechanical Engineering 119 (4), 438–444.

Guo, X., Kassab, G. S., 2003. Variation of mechanical properties along the length of the aorta in C57BL/6 mice. American Journal of Physiology - Heart and Circulatory Physiology 285, H2614–H2622.

Holzapfel, G., Gasser, T., Ogden, R., 2000. A new constitutive framework for arterial wall mechanics and a comparative study of material models. Journal of Elasticity 61, 1–48.

Huang, Y., Guo, X., Kassab, G. S., 2006. Axial nonuniformity of geometric and mechanical properties of mouse aorta is increased during postnatal growth. American Journal of Physiology - Heart and Circulatory Physiology 290 (2), H657–H664.

Machii, M., Becker, A. E., 1997. Morphologic features of the normal aortic arch in neonates, infants, and children pertinent to growth. The Annals of Thoracic Surgery 64 (2), 511–515.

Ogden, R., 1997. Non–Linear Elastic Deformations. Dover.

Ohayon, J., Mesnier, N., Broisat, A., Toczek, J., Riou, L., Tracqui, P., 2012. Elucidating atherosclerotic vulnerable plaque rupture by modeling cross substitution of ApoE$^{-/-}$ mouse

17

and human plaque components stiffnesses. Biomechanics and Modeling in Mechanobiology 11 (6), 801–813.

Reitman, J., Mahley, R., Fry, D., 1982. Yucatan miniature swine as a model for diet-induced atherosclerosis. Atherosclerosis 43 (1), 119–132.

Schwartz, C. J., Sprague, E. A., Kelley, J. L., Valente, A. J., Suenram, C. A., 1985. Aortic intimal monocyte recruitment in the normo and hypercholesterolemic baboon (*Papio Cynocephalus*). Virchows Archiv 405, 175–191.

Sáez, P., Peña, E., Martínez, M. A., 2014. A Structural Approach Including the Behavior of Collagen Cross-Links to Model Patient-Specific Human Carotid Arteries. Ann Biomed Eng 42, 1158–1169.

Teng, Z., Zhang, Y., Huang, Y., Feng, J., Yua, J., Lu, Q., Sutcliffe, M. P. F., Brown, A. J., Jing, Z., Gillard, J. H., 2014. Material properties of components in human carotid atherosclerotic plaques: A uniaxial extension study. Acta Biomat 10, 5055–5063.

Tracqui, P., Broisat, A., Toczek, J., Mesnier, N., Ohayon, J., Riou, L., 2011. Mapping elasticity moduli of atherosclerotic plaque in situ via atomic force microscopy. Journal of Structural Biology 174, 115–123.

Tsamis, A., Krawiec, J. T., Vorp, D. A., 2013. Elastin and collagen fibre microstructure of the human aorta in ageing and disease: a review. J R Soc Interface 27, 10(83).

Waffenschmidt, T., 2014. Modelling and simulation of adaptation and degradation in anisotropic biological tissues. Ph.D. thesis, Institut für Mechanik, Technische Universität Dortmund, http://hdl.handle.net/2003/31797.

Waffenschmidt, T., Menzel, A., 2014. Extremal states of energy of a double-layered thick-walled tube – Application to residually stressed arteries. Journal of the Mechanical Behavior of Biomedical Materials 29, 635–654.

Wagner, W. D., 1978. Risk factors in pigeons genetically selected for increased atherosclerosis susceptibility. Atherosclerosis 31 (4), 453–463.

Wells, S. M., Langille, B. L., Lee, J. M., Adamson, S. L., 1999. Determinants of mechanical

properties in the developing ovine thoracic aorta. American Journal of Physiology - Heart and Circulatory Physiology 277 (4), H1385–H1391.

Wong, L. C. Y., Langille, B. L., 1996. Developmental Remodeling of the Internal Elastic Lamina of Rabbit Arteries: Effect of Blood Flow. Circulation Research 78 (5), 799–805.

Table 1

Setting of material, structural, geometrical and loading parameters used throughout all the following computations. The fibre angle β is based on data from Ohayon et al. (2012), the geometry is based on data from Cilla et al. (2015) and it has been obtained from histological analysis performed after the mechanical tests.

Type	Symbol	Description	Value	Unit
Material	c	elastic constant	to be identified	$[kPa]$
	k_1	elastic constant	to be identified	$[kPa]$
	k_2	elastic constant	to be identified	$[-]$
Structural	β	fibre angle	48.47	$[deg]$
Geometrical	R_i	inner referential radius	0.38197	$[mm]$
	H	referential wall thickness thoracic aorta 10 [weeks]	0.1	$[mm]$
	H	referential wall thickness abdominal aorta 10 [weeks]	0.08	$[mm]$
Loading	λ_z	axial stretch	1.0	$[-]$

Table 2
Algorithmic box for the material parameter identification procedure.

---

(1) set up structural and geometrical parameters from Table 1 and collect these in pseudo-vector $\boldsymbol{\kappa} = [\beta, \, R_i, \, H, \, \lambda_z]$

(2) perform initial guess $\boldsymbol{\nu} = \boldsymbol{\nu}^0 = \left[c^0, \, k_1^0, \, k_2^0 \right]$ for the material parameters to be identified

(3) set objective function to $f(\boldsymbol{\nu}) = 0$

(4) identify material parameters as argument of minimum of objective function f
$$\boldsymbol{\nu}^{\min} = \arg\, \min_{\boldsymbol{\nu}} f\left(\boldsymbol{\nu}; \boldsymbol{\nu}^0, \boldsymbol{\kappa}\right) \;,$$

wherein $f(\boldsymbol{\nu})$ is determined by the algorithm for the pressure-driven case and the minimisation can be performed by, e.g., the Matlab `fmincon`-optimisation-function

---

Table 3
Algorithmic box for the pressure-driven deformation process were $h = 1.0e^{-8}$, $tol = 1.0e^{-8}$ and $w = 1.0$. All quantities are associated with t_{n+1}.

(1) given: internal pressure p_i^{exp} at time t_{n+1}

(2) perform initial guess $\lambda_{\theta_o} = \lambda_{\theta_o}^0$ for the outer circumferential stretch

(3) perform local Newton-Raphson iteration scheme

    (a) compute residual

        $r(\lambda_{\theta_o}) = p_i^{\text{exp}} - p_i(\lambda_{\theta_o})$

        wherein $p_i(\lambda_{\theta_o})$ is determined by the algorithm described below

    (b) compute linearisation of residual by means of forward difference scheme

        $\mathrm{d}r = \left[r(\lambda_{\theta_o} + h) - r(\lambda_{\theta_o})\right]/h$ with $h \ll 1$

    (c) Compute increment

        $\Delta\lambda_{\theta_o} = \mathrm{d}r/r$

    (d) compute update

        $\lambda_{\theta_o} \hookleftarrow \lambda_{\theta_o} - \Delta\lambda_{\theta_o}$

    (e) check tolerance with tol $\ll 1$

        if $|r| <$ tol go to 4.

        else go to 3. (a)

(4) compute objective function

    $f(\boldsymbol{\nu}) \hookleftarrow f(\boldsymbol{\nu}) + w\left[\lambda_{\theta_o} - \lambda_{\theta_o}^{\text{exp}}\right]^2$

Table 4
Algorithmic box for the determination of the internal pressure Waffenschmidt and Menzel (2014); Waffenschmidt (2014).

---

(1) given: material parameters $\boldsymbol{\nu} = [c, k_1, k_2]$, structural and geometrical parameters $\boldsymbol{\kappa} = [\beta, R_i, H, \lambda_z]$, see Table 1,

deformation in terms of the outer circumferential stretch λ_{θ_o} at time t_{n+1}

(2) calculate referential outer radius

$R_o = R_i + H$

(3) calculate current radii

$r_o = \lambda_{\theta_o} R_o$

$r_i = \sqrt{r_o^2 - \left[R_o^2 - R_i^2\right]/\lambda_z}$

(4) apply $m = 3$-point Gaussian quadrature rule with quadrature points
$\xi_j = \left\{-\sqrt{3/5} \ 0 \ \sqrt{3/5}\right\}$ and weights $w_j = \left\{5/9 \ 8/9 \ 5/9\right\}$:

loop over number of quadrature points $j = 1, \ldots, m$

(a) calculate current radius

$r_j = \left[\left[r_i + r_o\right] + \xi_j \left[r_o - r_i\right]\right]/2$

(b) calculate referential radius

$R_j = \sqrt{\lambda_z \left[r_j^2 - r_i^2\right] + R_i^2}$

(c) calculate circumferential stretch

$\lambda_{\theta j} = r_j / R_j$

(d) calculate radial and circumferential stresses

$\sigma_{rrj} = c\,\lambda_{\theta j}^{-2}\,\lambda_z^{-2}$

$\sigma_{\theta\theta j} = c\,\lambda_{\theta j}^2 + 4\cos^2\left(\beta\right) k_1\,\lambda_{\theta j}^2\,E\exp\left(k_2\,\langle E\rangle^2\right)$

with $E = \lambda_z^2 \sin(\beta)^2 + \lambda_{\theta j}^2 \cos(\beta)^2 - 1$ by means of equations (18, 19)

calculate internal pressure

$p_i \approx \left[r_o - r_i\right]/2 \sum_{j=1}^{m} \left[\sigma_{\theta\theta j} - \sigma_{rrj}\right] w_j / r_j$

Table 5

Identified material parameters by means of the pressure-driven material parameter identification procedure.

|		diseased ApoE$^{-/-}$ mice				healthy control mice			
	[weeks]	10	20	30	40	10	20	30	40
Upper aorta	c [kPa]	13.92	54.83	85.38	89.74	32.09	35.80	39.87	18.29
	k_1 [kPa]	116.70	155.08	167.36	160.41	128.96	125.49	142.81	113.99
	k_2 [−]	1.20	1.33	1.21	2.69	1.00	1.19	1.14	1.57
Lower aorta	c [kPa]	32.51	49.31	116.15	142.56	40.50	22.36	40.69	33.81
	k_1 [kPa]	123.90	142.81	171.43	158.89	136.79	118.49	150.56	131.24
	k_2 [−]	1.06	1.19	1.42	2.71	0.95	1.57	0.90	1.37
Abdominal aorta	c [kPa]	34.38	67.61	108.09	105.12	48.10	29.62	62.78	49.29
	k_1 [kPa]	122.75	144.24	173.31	180.15	132.20	112.06	150.12	147.65
	k_2 [−]	1.99	1.89	1.89	3.81	2.11	2.52	2.18	2.33
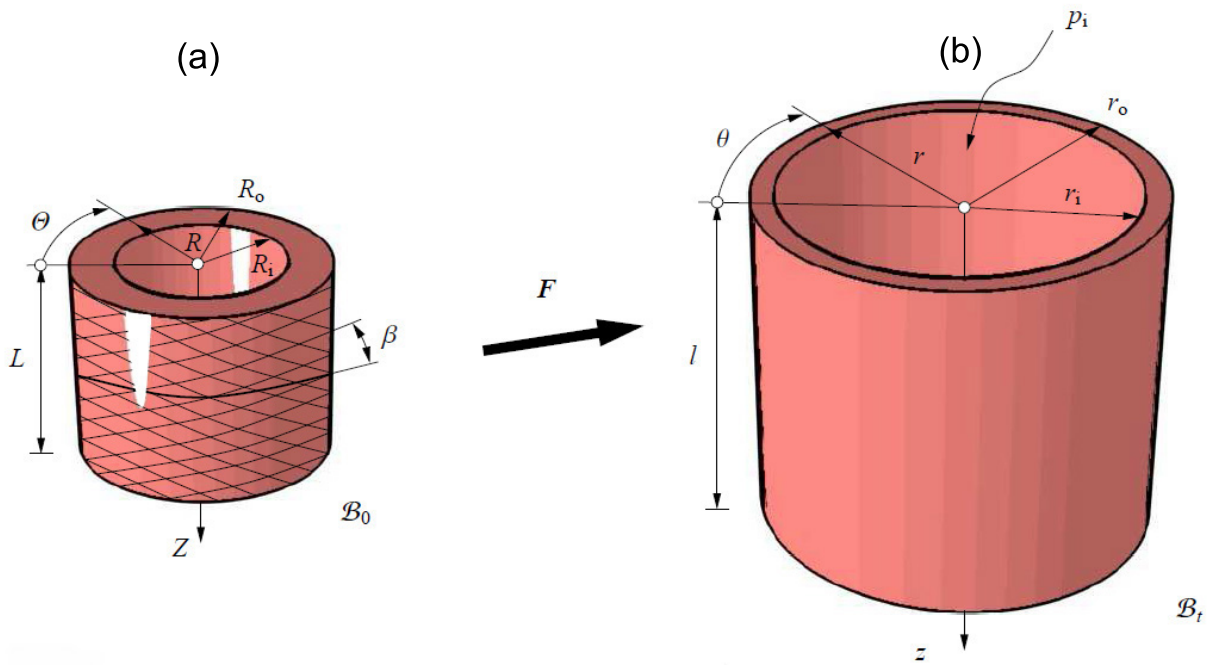
Fig. 1. Deformation modes of a thick-walled cylindrical tube: inflation (internal pressure p_i) and axial extension (axial stretch $\lambda_z = l/L$); arterial wall reinforced by two families of fibres with fibre angle β defined in (a) a stress-free reference configuration $\mathcal{B}_0$ defined with respect to the circumferential direction; (b) residually stressed and loaded current configuration $\mathcal{B}_t$.
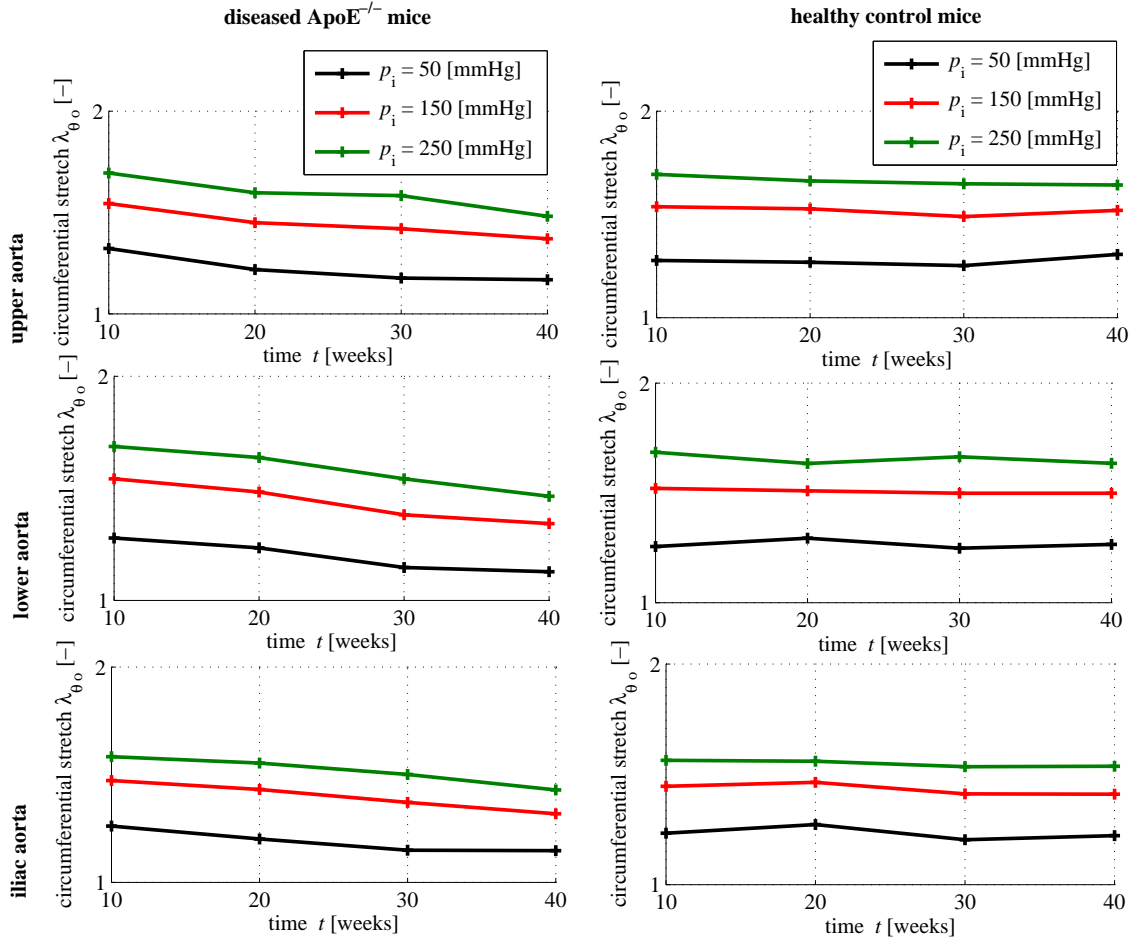
Fig. 2. Experimentally obtained circumferential stretch with respect to different stages of ageing at three chosen pressure levels, i.e. $p_i = \{50, 150, 250\}$ $[mmHg]$. The left column corresponds to the diseased ApoE$^{-/-}$ mice, the right column corresponds to the healthy control mice. The three different rows top, middle, bottom are associated with different locations over the length of the considered arterial specimen (Cilla et al., 2015).
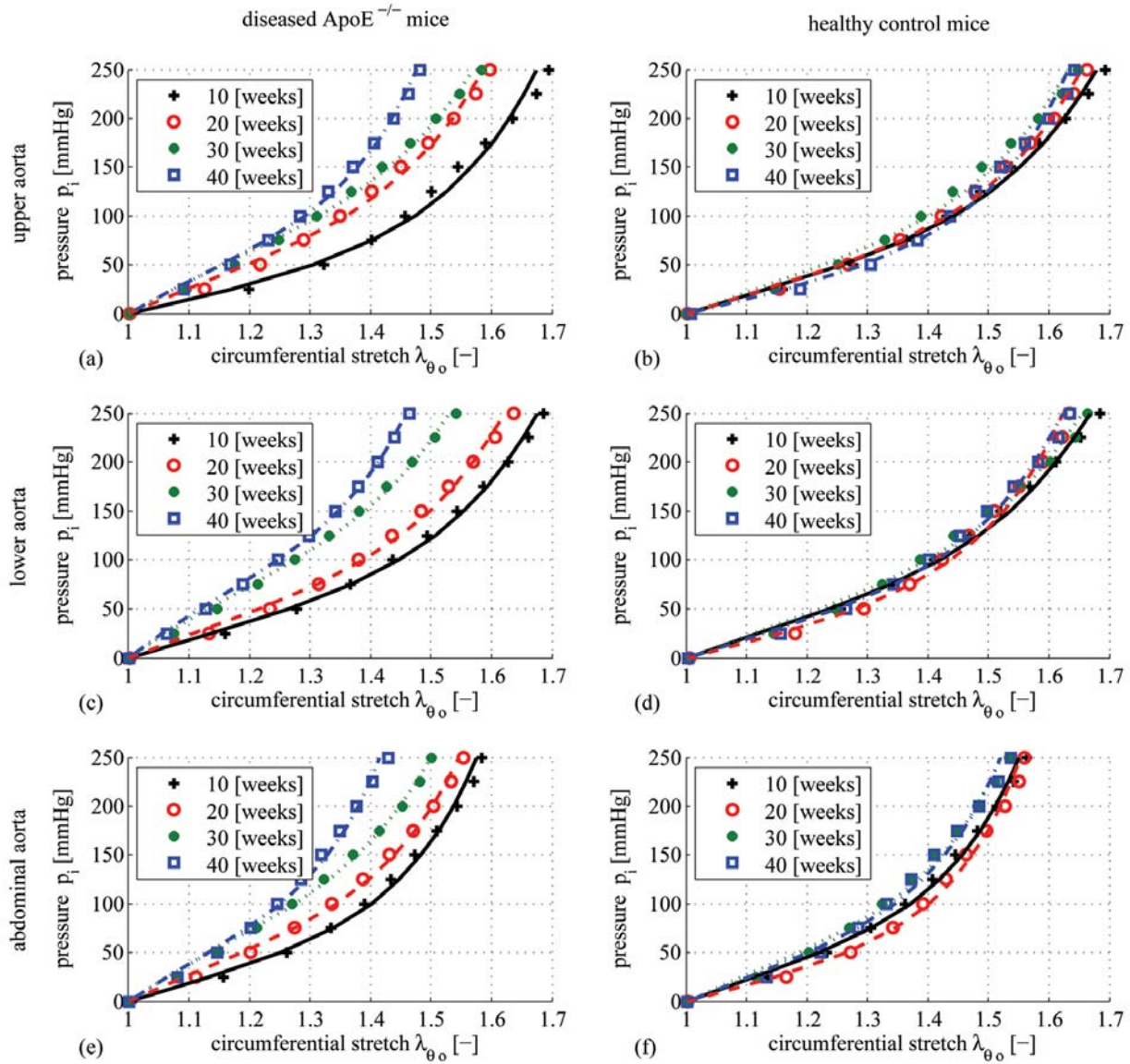
Fig. 3. Fitted experimental data based on the material parameter identification procedure. The discrete points represent the original experimental data from (Cilla et al., 2015), the lines the associated (simulated) fitting. The material parameter identification procedure is based on a sequential optimisation of three material parameters c, k_1 and k_2: in a first step parameter c is identified with $k_1 = $ const and $k_2 = $ const using the first two experimental data points, in a second step k_1 and k_2 are identified with $c = $ const using all experimental data points.
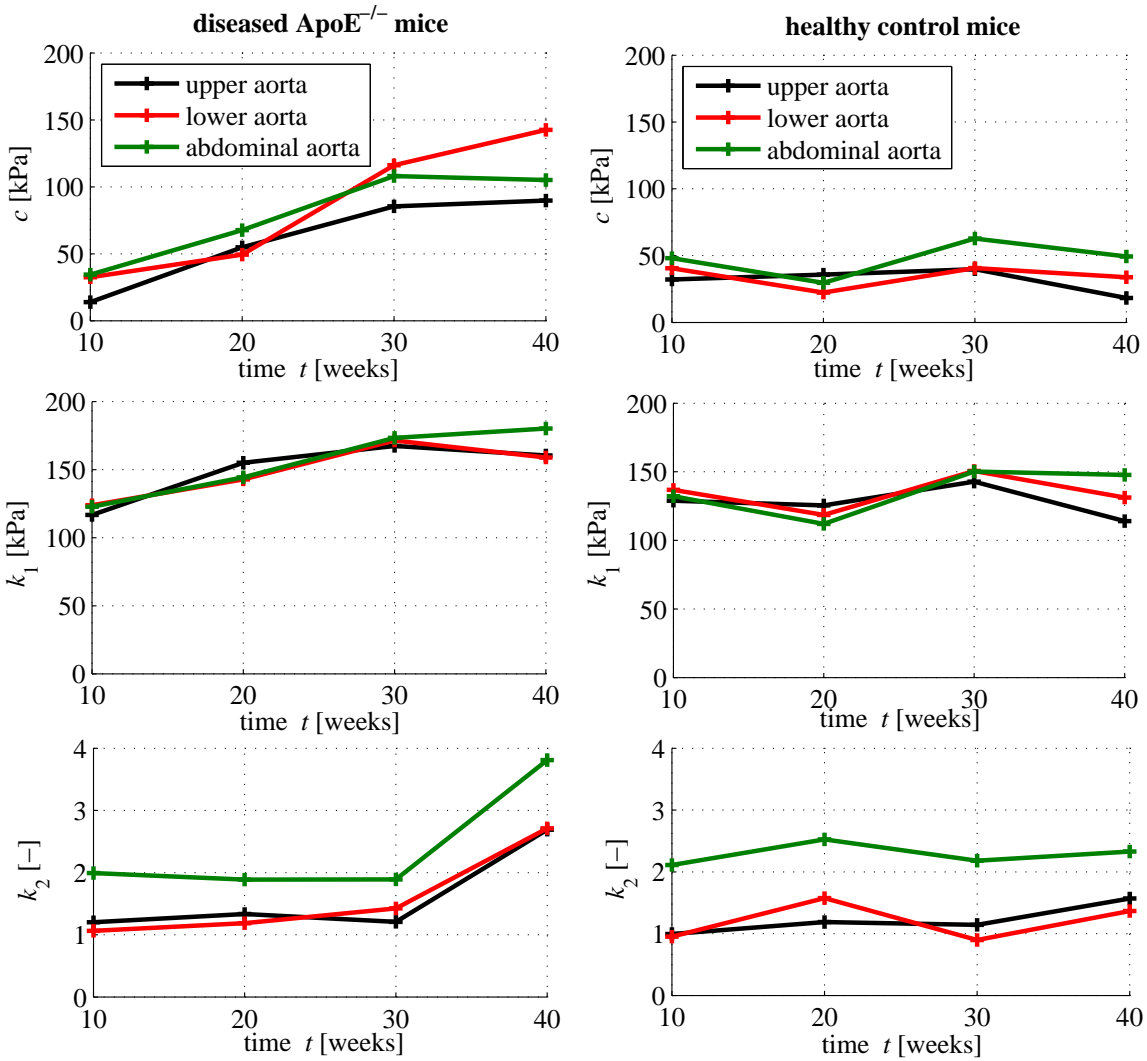
Fig. 4. Material parameter evolution for the stress-driven (pressure-driven) parameter identification procedure plotted over time, associated values given in Table 5. The left column corresponds to the diseased ApoE$^{-/-}$ mice, the right column corresponds to the healthy control mice.